The Astrophysical Journal, 944:53 (10pp), 2023 February 10 https://doi.org/10.3847/1538-4357/acb0d3

Relativistic Correction to the *r*-mode Frequency in Light of Multimessenger Constraints

Suprovo Ghosh, Dhruv Pathak, and Debarati Chatterjee
Inter-University Centre for Astronomy and Astrophysics, Pune University Campus, Pune—411007, India; suprovo@iucaa.in
Received 2022 September 26; revised 2022 December 12; accepted 2023 January 4; published 2023 February 13

Abstract

The *r*-mode oscillations of rotating neutron stars are promising candidates for continuous gravitational-wave (GW) observations. The *r*-mode frequencies for slowly rotating Newtonian stars are well known and independent of the equation of state (EOS), but for neutron stars several mechanisms can alter the *r*-mode frequency for which the relativistic correction is dominant and relevant for most of the neutron stars. The most sensitive searches for continuous GWs are those for known pulsars for which GW frequencies are in targeted narrow frequency bands of a few hertz. In this study, we investigate the effect of several state-of-the-art multimessenger constraints on the *r*-mode frequency for relativistic, slowly rotating, barotropic stars. Imposing these recent constraints on the EOS, we find that the *r*-mode frequency range is slightly higher than that from the previous study and the narrowband frequency range can increase by up to 25% for the most promising candidate PSR J0537−6910 depending on the range of compactness. We also derive universal relations between *r*-mode frequency and dimensionless tidal deformability that can be used to estimate the dynamical tide of the *r*-mode resonant excitation during the inspiral signal. These results can be used to construct the parameter space for *r*-mode searches in GW data and also constrain the nuclear EOS following a successful *r*-mode detection.

Unified Astronomy Thesaurus concepts: Neutron stars (1108); Gravitational wave sources (677); Pulsars (1306)

1. Introduction

Gravitational waves (GWs) can drive various modes of oscillation in a rotating neutron star (NS) unstable (Chandrasekhar 1970; Friedman & Schutz 1978). The *r*-mode is a toroidal mode of fluid oscillation for which the restoring force is the Coriolis force. For any rotating star, *r*-modes can become unstable to GW emission via the Chandrasekhar–Friedman–Schutz mechanism (Andersson 1998, 2003). This instability can explain the spin-down of hot and young NSs (Lindblom et al. 1998; Andersson et al. 1999; Alford & Schwenzer 2014), as well as old, accreting NSs in low-mass X-ray binaries (Ho et al. 2011), and provides a plausible explanation for the absence of very fast-rotating NSs in nature. Although shear and bulk viscosity of the NS matter can damp these oscillation modes (Lindblom & Owen 2002; Chatterjee & Bandyopadhyay 2006, 2007), while spinning down, NSs can enter a region of temperature and rotational frequency in which viscosity cannot damp the *r*-mode and the mode grows to a large amplitude, leading to GW emission (Lindblom et al. 1998).

Because of its astrophysical significance (Abbott et al. 2022), there have been recent searches for continuous GW emission speciically from *r*-modes using the LIGO–Virgo–Kagra (LVK) global network of GW detectors (Acernese et al. 2014; Aasi et al. 2015; Abbott et al. 2016; Akutsu et al. 2021). A search for GWs from *r*-modes in the Crab pulsar was carried out by Rajbhandari et al. (2021) and from PSR J0537 by Fesik & Papa (2020a, 2020b) and the LVK collaboration (Abbott et al. 2021). No GWs were detected in these searches, but upper limits on GW amplitude were obtained.

As the *r*-modes are rotationally restored stellar oscillations, their frequency is proportional to the rotation frequency (Papaloizou & Pringle 1978) for slowly rotating stars. If the targeted pulsar rotational frequency is known from electromagnetic data, the GW searches are done in a relatively narrow frequency band obtained from theoretical estimates (Caride et al. 2019). The *r*-mode frequency for a slowly and uniformly rotating Newtonian star in the perfect fluid approximation is found to be independent of the equation of state (EOS; Provost et al. 1981),

$$\kappa \equiv \frac{\sigma_R}{\Omega} = \frac{2m}{l(l+1)}, \tag{1}$$

where σ_R is the *r*-mode frequency in the corotating frame, Ω is the rotational angular velocity of the star, and l and m are the spherical harmonic indices. In the inertial frame, the frequency is given by $f = |(\kappa - m)\Omega|$.

For NSs, dominant factors influencing the *r*-mode frequency are relativistic effects (Lockitch et al. 2000, 2003; Idrisy et al. 2015) and rapid rotation (Lindblom et al. 1999; Yoshida et al. 2005). There are several other factors like the presence of solid crust (Levin & Ushomirsky 2001), stratification (Yoshida & Lee 2000; Passamonti et al. 2009), magnetic field (Ho & Lai 2000; Rezzolla et al. 2000, 2001a, 2001b; Morsink & Rezania 2002), or superfluidity in the core (Lindblom & Mendell 2000; Andersson & Comer 2001) that might affect the *r*-mode frequency, but their effect was found to be negligible for most stars (Idrisy et al. 2015). Rapid rotation can increase the value of κ by ∼6% for the fastest-rotating stars (Idrisy et al. 2015). But since this correction is of the order $(\Omega/\Omega_K)^2$, where Ω_K is the Keplerian frequency, the rotational corrections become negligible for slowly spinning stars. Lockitch et al. (2000, 2003) first derived the perturbation equations to solve for *r*-mode frequency for relativistic barotropic stars and calculated them using only polytropic EOSs. Later Idrisy et al. (2015) calculated the same for some tabulated EOSs. They sampled 14 EOSs that support a maximum mass of at least 1.85 $M_\odot$ and obtained the universal relation between *r*-mode frequency and compactness (Figure 3

in Idrisy et al. 2015) as

$$\kappa = 0.627 + 0.079(M/R) - 2.25(M/R)^2. \quad (2)$$

Since this work, there have been several recent multimessenger observations of NSs that have put constraints on the NS EOS. The detection of GWs from the binary NS merger GW170817 (Abbott et al. 2017, 2018, 2019, 2020b), the NICER measurement of mass and radius of pulsars (Miller et al. 2019, 2021; Riley et al. 2019, 2021) have been extensively used to constrain the nuclear EOS (Annala et al. 2018; Dietrich et al. 2020; Traversi et al. 2020; Biswas et al. 2021; Legred et al. 2021; Pang et al. 2021; Ghosh et al. 2022). The maximum observed mass of pulsars is also updated to around 2.08 $M_\odot$ (Fonseca et al. 2021). These multimessenger constraints (Abbott et al. 2020b) have ruled out with good confidence several tabulated EOSs that were used in Idrisy et al. (2015). Although in the universal relation given by Equation (2) Idrisy et al. (2015) were able to fit κ more accurately over the range of compactness of real physical interest, they did not impose two important physical constraints on the r-mode frequency: (i) in the Newtonian limit when $M/R \longrightarrow 0$, then $\kappa = 2/3(\sim 0.667)$ for $l = m = 2$ mode; and (ii) the linear coefficient in the fit relation should be negative; otherwise, it will imply that the r-mode frequency increases with an increase in compactness up to a certain value (Lockitch et al. 2000).

In this study, we calculate the r-mode frequency for 15 tabulated EOSs sampled from Idrisy et al. (2015) and Abbott et al. (2020b) that are consistent with recent multimessenger observations of NSs. Along with these tabulated EOSs, we also consider a posterior for the EOS from Legred et al. (2021), employing a nonparametric EOS model based on Gaussian processes and combining information from pulsar masses, NICER observation of the mass–radius relation, and GW observations of binary NS mergers. The advantages of this nonparametric EOS model are that this allows more model freedom in the EOS representation than any direct parameterization with a small number of parameters; can account for different degrees of freedom, including hyperonic, quark models, and phase transition; and is not subject to any systematic errors that arise with parameterized EOS families (Legred et al. 2021).

A couple of recent studies (Ma et al. 2021; Gupta et al. 2022) have also looked into the possible resonant r-mode detection in the inspiral phase of the binary mergers using the third-generation detector Einstein telescope (Punturo et al. 2010; Hild et al. 2011). The r-mode introduces an additional phase to the waveform model that is estimated from the r-mode frequency κ as a function of the dimensionless tidal deformability of the NS. Hence, for both of these sets of EOS models, we calculate the r-mode frequency as a function of dimensionless tidal deformability. We also give universal relations of the r-mode frequency with both the compactness and dimensionless tidal deformability, which will be useful to constrain the parameter space for searches for r-modes from both isolated pulsars and excitation during inspiral phase in binaries. In case GWs are detected from the r-mode oscillations, these universal relations can also be used to constrain the NS EOS.

The structure of the article is as follows: In Section 2, we describe the formalism of the structure of equilibrium configuration of a slowly and uniformly rotating star, relevant perturbation, and boundary equations. The details of the numerical scheme and their convergence are discussed in Section 3. We first test the scheme by comparing with the results of Idrisy et al. (2015) and Lockitch et al. (2003) for polytropic EOSs, then extend the analysis for our EOS models, and finally demonstrate the results of the investigation, including the universal relations, in Section 4. In Section 5 we discuss the main implications of this work.

2. Formalism

2.1. Equilibrium Configuration of a Slowly and Uniformly Rotating Star

We consider a slowly and uniformly rotating perfect fluid star with angular velocity Ω. The *slow-rotation* approximation requires that $\Omega \ll \Omega_K$, where Ω_K is the Keplerian frequency ($\propto\sqrt{M/R^3}$). In this slow-rotation approximation, the NS retains its spherical geometry, as the centrifugal deformations are an order Ω^2 effect (Hartle 1967). The equilibrium solution to the slowly and uniformly rotating star is obtained by solving the Einstein equations $G_{\alpha\beta} = 8\pi T_{\alpha\beta}$ using the line element given by (Lockitch et al. 2000)

$$ds^2 = -e^{2\nu(r)}dt^2 + e^{2\lambda(r)}dr^2 + r^2 d\theta^2 + r^2\sin^2(\theta)d\phi^2 - 2\omega(r)r^2\sin^2(\theta)dtd\phi, \quad (3)$$

where $\omega(r)$ is the rotational frame dragging inside the star. The energy momentum tensor for the perfect fluid is given by

$$T_{\alpha\beta} = (\varepsilon + p)u_\alpha u_\beta + p g_{\alpha\beta}. \quad (4)$$

Here ε and p are the total energy density and pressure of the fluid, respectively, measured by an observer comoving with the 4-velocity

$$u^\alpha = e^{-\nu}(t^\alpha + \Omega\phi^\alpha), \quad (5)$$

where t^α and ϕ^α are the timelike and rotational killing vectors of the spacetime, respectively. Solving the Einstein equations for the metric and fluid variables, they reduce to Tolman–Oppenheimer–Volkov (TOV) equations:

$$\frac{dm(r)}{dr} = 4\pi\varepsilon(r)r^2,$$
$$\frac{dp(r)}{dr} = -\frac{[p(r)+\varepsilon(r)][m(r)+4\pi r^3 p(r)]}{r(r-2m(r))}. \quad (6)$$

We also obtain the equations for the metric functions $\nu(r)$ and $\lambda(r)$ as

$$\frac{d\nu(r)}{dr} = -\frac{1}{\varepsilon + p}\frac{dp(r)}{dr},$$
$$e^{-2\lambda} = 1 - \frac{2m(r)}{r}. \quad (7)$$

For a given EOS $p = p(\varepsilon)$, the TOV Equations (6) are integrated from the center of the star to the surface using the boundary conditions of vanishing mass, $m|_{r=0} = 0$, at the center of the star and a vanishing pressure, $p|_{r=R} = 0$, at the surface ($r = R$). For the metric function $\nu(r)$, we start the integration from $r = 0$ with $\nu(0) = 0$, and the solution must match the exterior solution at the surface. We implement it by making the

following variable change (Glendenning 2012):

$$\nu(r) \longrightarrow \nu(r) - \nu(R) + \frac{1}{2}\ln\left(1 - \frac{2M}{R}\right), \tag{8}$$

where $M = m(R)$ is the total mass of the star.

For the slowly rotating equilibrium configuration, in addition to the TOV equations, we need to solve an equation for the other metric function $\omega(r)$ given by the Hartle equation (Hartle 1967):

$$\frac{1}{r^4}\frac{d}{dr}\left(r^4 j\frac{d\bar{\omega}}{dr}\right) + \frac{4}{r}\frac{dj}{dr}\bar{\omega} = 0, \tag{9}$$

where

$$\bar{\omega}(r) = \Omega - \omega(r). \tag{10}$$

Parameter $j(r)$ is defined in terms of the metric functions as

$$\begin{aligned} j(r) &= e^{-(\nu+\lambda)} \quad \text{for } r \leqslant R, \\ &= 1 \quad \text{for } r > R. \end{aligned} \tag{11}$$

The differential Equation (9) for $\omega(r)$ can be integrated from $r = 0$ with an arbitrary choice of the central value $\bar{\omega}(0)$ and a vanishing slope (Glendenning 2012). At the surface, it should match the exterior solution. From Equation (9), the exterior solution ($r > R$) is given by

$$\omega(r) = \frac{2J}{r^3}, \tag{12}$$

where J is the angular momentum of the star. At the surface, the corresponding boundary conditions should be matched,

$$\begin{aligned} J &= \frac{1}{6}R^4\left(\frac{d\bar{\omega}}{dr}\right)_R, \\ \Omega &= \bar{\omega}(R) + \frac{2J}{R^3}. \end{aligned} \tag{13}$$

Since $\bar{\omega}(r)$ depends on the rotational frequency Ω, we normalize $\bar{\omega}(r)$ by Ω, $\bar{\omega}(r) \equiv \frac{\bar{\omega}(r)}{\Omega}$, and make $\Omega = 1$.

The tidal deformability parameter quantifies the degree of the tidal deformation effects due to the companion in coalescing binary NS systems during the early stages of an inspiral. It is defined as

$$\lambda = -\frac{Q_{ij}}{\varepsilon_{ij}}, \tag{14}$$

where Q_{ij} is the induced mass quadrupole moment of the NS and ε_{ij} is the gravitational tidal field of the companion. The dimensionless tidal deformability (Λ) can be obtained by solving a set of differential equations coupled with the TOV equations, and it is related to the dimensionless $l = 2$ tidal Love number k_2 (Flanagan & Hinderer 2008; Hinderer 2008) as

$$\Lambda = \frac{2}{3}k_2\left(\frac{R}{M}\right)^5. \tag{15}$$

2.2. Perturbation Equations

Here we consider the nonradial perturbations of these slowly rotating equilibrium models to linear order in Ω. Since the equilibrium spacetime is stationary and axisymmetric, we decompose our perturbations using the Lagrangian formalism into modes of the form $e^{i(\sigma t + m\phi)}$ (Lockitch et al. 2000). We express the perturbed configuration in terms of the set ($h_{\alpha\beta}$, ζ^α, $\delta\varepsilon$, δp). Since the perturbed energy density and pressure are scalar, they have polar parity and are given as

$$\delta\varepsilon = \delta\varepsilon(r)Y_l^m,\ \delta p = \delta p(r)Y_l^m. \tag{16}$$

The Lagrangian displacement vector is defined as

$$\begin{aligned} \zeta^\alpha = \frac{1}{i\kappa\Omega}\sum_{l=m}^{\infty}\Bigg(&\frac{1}{r}W_l(r)Y_l^m r^\alpha + V_l(r)\nabla^\alpha Y_l^m \\ &- iU_l(r)P_\nu^\alpha \epsilon^{\nu\beta\gamma\delta}\nabla_\beta Y_m^l \nabla_\gamma t \nabla_\delta r\Bigg)e^{i\sigma t}, \end{aligned} \tag{17}$$

where

$$P_\nu^\alpha = e^{\nu+\lambda}(\delta_\nu^\alpha - t_\nu\nabla^\alpha t), \tag{18}$$

and the comoving frequency is given by

$$\kappa\Omega \equiv \sigma + m\Omega. \tag{19}$$

The perturbation variables W_l and V_l have polar parity, and U_l has axial parity. In the Regge–Wheeler gauge the metric perturbation is given by

$$\begin{aligned} h_{\mu\nu} = Y_l^m e^{i\sigma t}\sum_{l=m}^{\infty} \\ \times\begin{bmatrix} H_{0,l}(r)e^{2\nu} & H_{1,l}(r) & h_{0,l}(r)\left(\frac{m}{\sin(\theta)}\right) & ih_{0,l}(r)\sin(\theta)\partial_\theta \\ H_{1,l}(r)e^{2\nu} & H_{2,l}(r) & h_{1,l}(r)\left(\frac{m}{\sin(\theta)}\right) & ih_{0,l}(r)\sin(\theta)\partial_\theta \\ \text{symm} & \text{symm} & r^2K_l(r) & 0 \\ \text{symm} & \text{symm} & 0 & r^2\sin^2(\theta)K_l(r) \end{bmatrix}, \end{aligned} \tag{20}$$

which contains both axial ($h_{0,l}$, $h_{1,l}$) and polar ($H_{0,l}$, $H_{1,l}$, $H_{2,l}$, K_l) parity components. We obtain the perturbation equations by requiring $\delta G_{\alpha\beta} = 8\pi\delta T_{\alpha\beta}$ term by term. Since we are considering up to order Ω variables and the displacement vector in Equation (17) already has a $\kappa\Omega$ term, we only keep the zeroth-order perturbation variables. The variables can be grouped depending on their order of dependence on the rotational frequency Ω. The relevant variables that are zeroth order in Ω are W_l, V_l, U_l, $H_{1,l}$, and $h_{0,l}$. Because $h_{1,l}$ is an order Ω variable, we drop the "0" subscript and write $h_{0,l}$ as h_l. The relevant $O(1)$ equations are given by

$$H_{1,l} + \frac{16\pi(\varepsilon + p)}{l(l+1)}e^{2\lambda}rW_l = 0, \tag{21}$$

$$V_l[l(l+1)(\epsilon + p)] - e^{-(\nu+\lambda)}[(\epsilon + p)e^{\nu+\lambda}W_l]' = 0, \tag{22}$$

$$\begin{aligned} r^2h_l'' - r^2(\nu' + \lambda')h_l' + [(2 - l^2 - l)e^{2\lambda} \\ - r(\nu' + \lambda') - 2]h_l - 4r(\nu' + \lambda')U_l = 0, \end{aligned} \tag{23}$$

where a prime denotes a derivative with respect to r. We have used Equation (21) to eliminate the variable $H_{1,l}$ in favor of W_l.

To close the system of equations, we obtain two other independent equations that arise at $O(\Omega)$, which enforces the conservation of vorticity in constant entropy surfaces

$$\begin{aligned} 0 = &[l(l+1)\kappa\Omega(h_l + U_l) - 2m\bar{\omega}U_l] \\ &+ (l+1)Q_l[(2\bar{\omega} + \mu)W_{l-1} - 2(l-1)\bar{\omega}V_{l-1}] \\ &- Q_{l+1}[(2\bar{\omega} + \mu)W_{l+1} + 2(l+2)\bar{\omega}V_{l+1}], \end{aligned} \tag{24}$$

$$
\begin{aligned}
0 = {} & (l-2)l(l+1)Q_{l-1}Q_l[-2\bar{\omega}rU'_{l-2} \\
& + 2(l-1)\bar{\omega}U_{l-2} + (l-3)\mu U_{l-2}] \\
& + (l+1)Q_l[(l-1)l\kappa\Omega rV'_{l-1} - 2ml\bar{\omega}rV'_{l-1} \\
& - 2l(l-1)\kappa\Omega r\nu' V_{l-1} + 2ml(l-1)\bar{\omega}V_{l-1} \\
& + m(l-3)l\mu V_{l-1}] - (l+1)Q_l \\
& \times [(l-1)l\kappa\Omega e^{2\lambda}W_{l-1} - 4\kappa\Omega r(\nu' + \lambda')W_{l-1}] \\
& + l(l+1)[m\kappa\Omega r(h'_l + U'_l) - 2m\kappa\Omega r\nu'(h_l + U_l) \\
& + ((l+1)Q_l^2 - lQ_{l+1}^2)(2\bar{\omega}rU'_l + 2\mu U_l)] \\
& + l(l+1)[m^2 + l(l+1)(Q_{l+1}^2 + Q_l^2 - 1)] \\
& \times (2\bar{\omega} + \mu)U_l - lQ_{l+1}[(l+1)(l+2)\kappa\Omega rV'_{l+1} \\
& + 2m(l+1)\bar{\omega}rV'_{l+1} - 2(l+1)(l+2)\kappa\Omega r\nu' V_{l+1}] \\
& - lQ_{l+1}[2m(l+1)(l+2)\bar{\omega}V_{l+1} \\
& + m(l+1)(l+4)\mu V_{l+1} - (l+1)(l+2)\kappa\Omega e^{2\lambda}W_{l+1} \\
& + 4\kappa\Omega r(\nu' + \lambda')W_{l+1}] \\
& + l(l+1)(l+3)Q_{l+1}Q_{l+2}[2\bar{\omega}rU'_{l+2} \\
& + 2(l+2)\bar{\omega}U_{l+2} + (l+4)\mu U_{l+2}],
\end{aligned}
\tag{25}
$$

where we have defined $\mu = re^{2\nu}(\bar{\omega}e^{-2\nu})'$. For the barotropic stars (which is the case for cold NSs), the conservation of vorticity gives rise to a mixing of axial and polar modes at zeroth order in Ω (Lockitch et al. 2000). This suggests that the modes of barotropic stars will generically be of a hybrid nature.

2.3. Boundary Conditions

In order to solve Equations (22)–(25), we need to apply the appropriate boundary conditions. The first boundary condition is also called the regularity condition, which says that the perturbation equations must be regular at the center of the star. To implement this boundary condition, we introduce a new variable $\tilde{P}_l$ corresponding to each perturbation variable P_l as

$$
P_l(r) = \left(\frac{r}{R}\right)^{l+q}\tilde{P}_l(r), \tag{26}
$$

where P_l is any one of the perturbation variables W_l, V_l, U_l, h_l. The prefactor $\left(\frac{r}{R}\right)^{l+q}$ provides for the condition of regularity at the origin. The axial parity variables (U_l, h_l) have $q = 1$, and polar parity variables (W_l, V_l) have $q = 0$ (Lockitch et al. 2003).

The next boundary condition comes from the fact that the Lagrangian perturbation of the pressure is zero at the surface of the star, which translates to

$$
W_l(R) = 0. \tag{27}
$$

Now h_l is the only variable defined outside the star where it follows

$$
\left(1 - \frac{2M}{r}\right)\frac{d^2h_l}{dr^2} - \left[\frac{l(l+1)}{r^2} - \frac{4M}{r^3}\right]h_l = 0. \tag{28}
$$

The solution of this equation is given by the hypergeometric function $h_l(r) = {}_2F_1(l-1,\ l+2; 2l+2; 2M/r)$ (Idrisy et al. 2015). The interior and exterior solutions are matched via the following boundary conditions:

$$
\lim_{\epsilon \to 0}[h_l(R-\epsilon) - h_l(R+\epsilon)] = 0, \tag{29}
$$

$$
\lim_{\epsilon \to 0}[h_l(R-\epsilon)h'_l(R+\epsilon) - h'_l(R-\epsilon)h_l(R+\epsilon)] = 0. \tag{30}
$$

3. Numerical Method

To get the r-mode frequencies, we need to solve the perturbation Equations (22)–(25) along with the boundary conditions (26), (27), (29), and (30). For a given EOS, solving the TOV Equation (6) and the Hartle Equation (9) gives the necessary equilibrium variables $p(r)$, $\varepsilon(r)$, $\nu(r)$, $\lambda(r)$, and $\omega(r)$. Since the perturbation equations are coupled in terms of l, we need to set an upper limit to our l value ($l_{\max}$) up to which we will solve these equations. As we are focusing on axial-led hybrid modes, we fix $l_{\max}$ to an odd value to get a closed system of equations (Idrisy et al. 2015). For this choice of axial-led hybrid modes, the perturbation variables have contributions only from the terms with (Lockitch et al. 2000)

$$
\begin{aligned}
&\text{axial parity } (h_l,\ U_l) \text{ with } l = m,\ m+2,\ m+4, \\
&\text{polar parity } (W_l,\ V_l) \text{ with } l = m+1,\ m+3,\ m+5.
\end{aligned}
$$

Hence, we solve for the eigenfunctions h_l, U_l, W_{l+1}, V_{l+1} for $l = m,\ m+2,\ \ldots$ and set others to zero.

Instead of integrating the coupled perturbation equations, we adopt a spectral method using the Chebyshev polynomials to find the eigenfrequency κ similar to Lockitch et al. (2003) and Idrisy et al. (2015). We express our system of ordinary differential equations in terms of the sum of basis functions, Chebyshev polynomials in our case, and using some useful identities, we reduce these differential equations to a system of algebraic equations, which is then solved using root-finding techniques to get the eigenfrequency.

3.1. Chebyshev Polynomials

The Chebyshev polynomials of the first kind are defined in the $[-1, 1]$ range by

$$
T_i(y) = \cos(i\ \arccos(y)). \tag{31}
$$

Any function $S(y)$ expanded in terms of Chebyshev polynomials is given by

$$
S(y) = \sum_{i=0}^{i_{\max}} s_i T_i(y) - \frac{1}{2}s_0, \tag{32}
$$

where

$$
\begin{aligned}
s_i = \frac{2}{i_{\max}}\sum_{j=0}^{i_{\max}+1}\Bigg\{ & S\left[\cos\left(\frac{\pi\left(j+\frac{1}{2}\right)}{i_{\max}}\right)\right] \\
& \times \cos\left(\frac{\pi i\left(j+\frac{1}{2}\right)}{i_{\max}}\right)\Bigg\}.
\end{aligned}
\tag{33}
$$

Since our variable r is in domain $[0, R]$, we define a new variable $y = 2\left(\frac{r}{R}\right) - 1$. Now, choosing $i_{\max}$ is a trade-off, as increasing $i_{\max}$ gives better convergence, but it also increases the number of equations to solve. Along with this, we also make use of two other identities for Chebyshev polynomials involving derivatives of a function and product of functions.

If f_l' and f_l are the Chebyshev coefficients of the derivative of a function and the function itself, respectively, then they are related by

$$f'_{l,i} - f'_{l,i+2} = 2(i+1)f_{l,i+1}. \tag{34}$$

If b_i and $f_{l,i}$ are the Chebyshev coefficients of a background function $B(y)$ and perturbation variable $F_l(y)$, respectively, then the Chebyshev coefficients for their products are given by

$$\pi_{l,i} = \sum_{j=0}^{i_{\max}} [b_{i+j} + \Theta(j-1)b_{|i-j|}]f_{l,j}, \tag{35}$$

where Θ is the step function.

After imposing the regularity condition (26), each term in the perturbation equation can be written in terms of a background function ($B(r)$), which depends on the star equilibrium profiles and a foreground function ($\tilde{F}_l(r)$), which are the perturbation variables. Since f_l' and f_l are connected by Equation (34), we only have f_l as our unknown functions. Now we expand each of them in terms of the Chebyshev polynomials and simplify them using the identities (33)–(35). We also rewrite the boundary conditions in the same way.

After expanding all the perturbation equations in terms of Chebyshev polynomials, we extract the coefficients using the identities (33)–(35). This leads to a system of $2(l_{\max}-3)i_{\max}$ linear equations for κ with the unknown functions f_l. We represent the system of equations as

$$A(\kappa)x = 0, \tag{36}$$

where x is the vector of f_l values containing Chebyshev coefficients of the perturbation variables. To incorporate the boundary conditions, we replace the equation that came from the highest-order Chebyshev coefficient $f_{i_{\max}}$ by a boundary condition (Idrisy et al. 2015). For example, to implement the boundary condition $W_l(R) = 0$ (Equation (27)), we replace the highest-order Chebyshev coefficient $f_{i_{\max}}$ as

$$w_{l_{i\max}} = \frac{1}{2}w_{l_0} - \sum_{i=0}^{i_{\max}-1} w_{l_i}, \tag{37}$$

where w_l values are the Chebyshev coefficients of the variable W_l. We have used, at at $r = R$, $y = 1$ and $T_i(1) = 1\,\forall i$.

3.2. Root-finding Method

To find the eigenfrequency κ, we set $\det(A(\kappa)) = 0$. This leads to a very high degree of polynomial in κ for any reasonable value of $l_{\max}$ and $i_{\max}$ that is not solvable by any standard root-finding techniques. We use the second root-finding algorithm given in Idrisy et al. (2015), which uses the singular value decomposition (SVD) of the matrix A, SVD $(A) = U\Sigma V$. We vary κ in the physically possible range (0.67–0.4) and look for the value of κ that results in the smallest value for the last element on the diagonal of Σ. For a particular $l_{\max}$ and $i_{\max}$, we find several roots for κ. The way to determine the correct root is to start at small values of $l_{\max}$ and $i_{\max}$ and increase them step by step. We will always converge to the correct root for any $l_{\max}$ and $i_{\max}$, while the others will change unpredictably.

In Figure 1 we plot the last diagonal element in SVD of the matrix A (denoted by ζ) versus κ for different choices of $i_{\max}$ with fixed $l_{\max}$ and vice versa for an $n = 1$ polytrope with compactness of 0.153. For the polytropes we get convergence

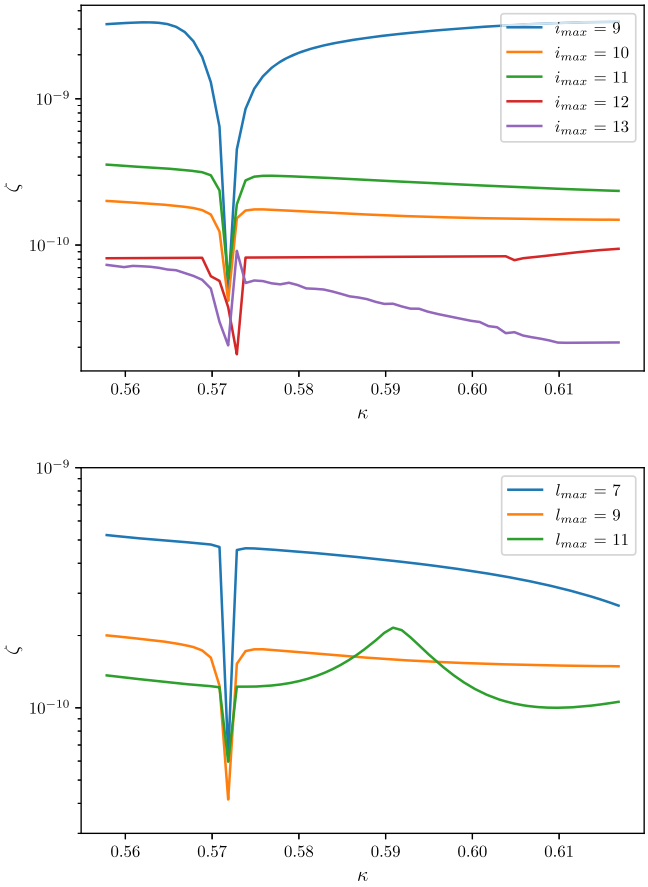

Figure 1. Convergence of the root with changing $l_{\max}$ and $i_{\max}$. The top panel shows the convergence for varying $i_{\max}$ while $l_{\max} = 9$, and the bottom panel shows convergence for varying $l_{\max}$ for $i_{\max} = 10$.

at minima of $l_{\max} = 7$ and $i_{\max} = 9$, and the convergence stops above $l_{\max} = 13$ and $i_{\max} = 13$. For both polytropes and realistic EOSs, we get convergence up to three orders after the decimal place. Sometimes, the converged root will vary in the third decimal place with different $l_{\max}$ and $i_{\max}$. We take the statistical mode of the roots for different combinations of $l_{\max}$ and $i_{\max}$.

4. Results

4.1. Polytropic EOS

For the Newtonian stars, the $l = m = 2$ r-mode is the one expected to dominate the GW radiation from the hot and fast-rotating NSs (Lindblom et al. 1998; Andersson et al. 1999). However, Lockitch et al. (2000) showed that for the relativistic barotropes pure $l = m = 2$ does not exist. The corresponding modes are axial-led hybrid modes with $m = 2$. To test the accuracy of our numerical code, we first consider the case for polytropic EOSs and compare our results with previous studies (Lockitch et al. 2003; Idrisy et al. 2015). In Figure 2, we plot the r-mode frequency as a function of compactness for a uniform-density star model or $n = 0$ polytropic EOS and compare it with Figure 1 of Lockitch et al. (2003). We get a significant match, and the relative error is around 0.1%–0.7%. In Figure 3, we plot the r-mode frequency as a function of compactness for an $n = 1$ polytropic EOS along with the quadratic fit relation between r-mode frequency and compactness given by Equation (69) in Idrisy et al. (2015). In this case,

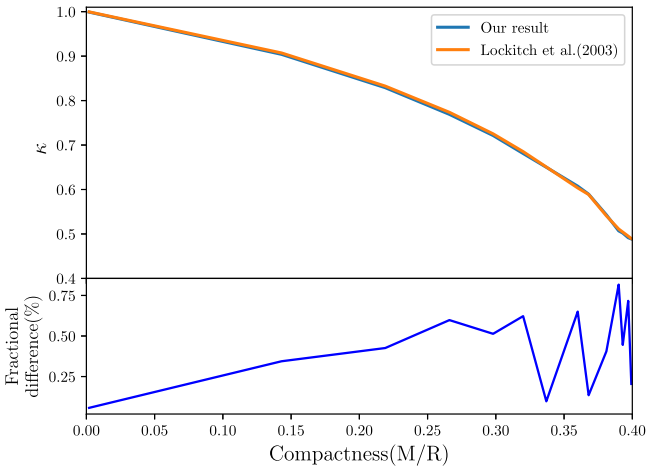

Figure 2. Normalized eigenfrequency κ/κ_N of $m = 2$ mode with their Newtonian counterparts for a uniform-density star as a function of compactness. Relative differences are shown in the bottom panel.

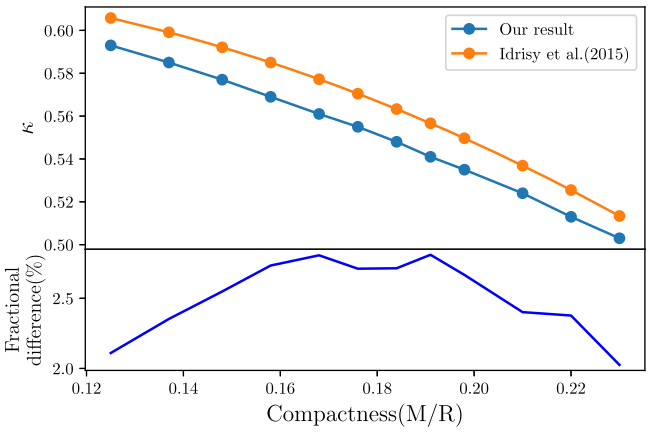

Figure 3. Eigenvalue κ for equilibrium stars of an $n = 1$ polytrope for different compactness. Relative differences are shown in the bottom panel.

we see a greater deviation (around 2%–3%) in the r-mode frequency from the results in Idrisy et al. (2015). We discuss the implications and possible reasons for this difference in Section 5.

In Figure 4, we show the best linear and quadratic model fits using the least-squares method to our results. For quadratic models, we also use a second model where the zeroth-order term of the polynomial is fixed to 2/3 to constrain the fact that as $M/R \to 0$ we reach the Newtonian limit, where the r-mode frequency for the $l = m = 2$ mode is given by

$$\kappa_N = \frac{2}{m+1} = 2/3.$$

From the R^2 value of the fits, we see that any quadratic model is a better fit than the linear model. Hence, we use the quadratic model, which satisfies the Newtonian limit

$$\kappa = 0.667 - 0.461C - 1.129C^2. \quad (38)$$

We also see that, along with the negative quadratic term, we also have the linear term negative in our fit Equation (38). This also satisfies the physical constraint that the r-mode frequency should decrease as we increase compactness (Lockitch et al. 2000),

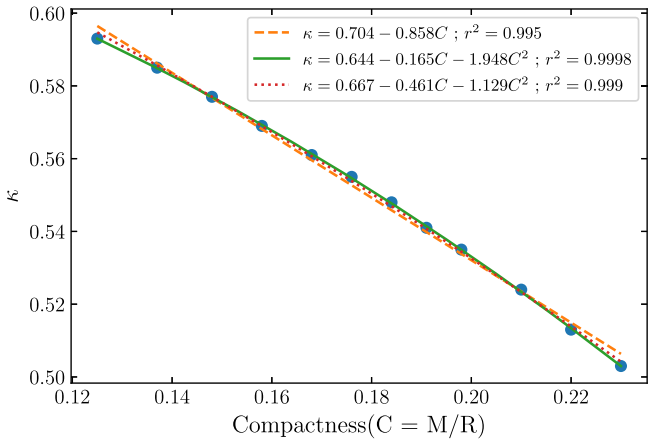

Figure 4. Linear and quadratic fits to κ vs. compactness results for equilibrium stars of an $n = 1$ polytrope.

unlike Equation (69) in Idrisy et al. (2015), which implies that κ increases with increasing compactness for $M/R < 0.10$ owing to the positive linear term.

4.2. Realistic Equations of State

4.2.1. Tabulated Equation of State

For realistic EOSs, Idrisy et al. (2015) considered 14 EOSs under the constraint that the EOS could support a minimum of 1.85 $M_\odot$. From the recent observations, the heaviest known pulsar PSR J0740+6620 has a maximum mass of $2.08^{+0.07}_{-0.07}$ $M_\odot$ (Fonseca et al. 2021). Taking an upper limit of the 1σ confidence interval of this maximum observed pulsar mass, we only consider EOSs that support a minimum of a 2.01 $M_\odot$ NS, which rules out three EOSs—GNH3, BBB2, and ALF4 used in Idrisy et al. (2015). In addition, the recent analyses of the GW170817 event (Abbott et al. 2019) apply a constraint on the upper bound of the effective tidal deformability $\tilde{\Lambda} < 720$ (Tong et al. 2020) using the PhenomPNRTwaveform model and low-spin highest posterior density interval for tidal deformability. Using these multimessenger observations of NSs, two very stiff EOSs (MS1, MS1b) considered in Idrisy et al. (2015) have been ruled out with good confidence (Abbott et al. 2020b; Biswas 2022). Along with the nine remaining EOSs from Idrisy et al. (2015), we consider six additional EOSs that satisfy the multimessenger constraints. Out of these additional six EOSs, one model, QHC19 (Baym et al. 2019), incorporates a transition between a hadronic phase in the crust and a quark matter phase in the core, and one other EOS model, CMF5 (Dexheimer & Schramm 2008), includes nucleons and hyperons. The other EOS models describe purely nucleonic matter. All our EOS tables are obtained from either COMPOSE (Oertel et al. 2017a, 2017b) or an EOS catalog from Özel & Freire (2016) used in LALSuite (LIGO Scientific Collaboration 2018). For the EOS tables obtained from COMPOSE we use their first-order interpolation option (Oertel et al. 2017b), and for the tables from Özel & Freire (2016) we use standard cubic spline interpolation (Abbott et al. 2020b). All the EOSs with their maximum mass and radius at 1.4 $M_\odot$ are listed in Table 1.

We compute the r-mode frequency κ for these EOS models for a range of compactness varying from 0.1 to a maximum of 0.31. Although this range of compactness is the same as used in

Table 1
List Of All The Tabulated EOSs With Corresponding Maximum Mass (in $M_\odot$), Radius for 1.4 $M_\odot$ Star (in km), κ for a Compactness of 0.15 (Along with the Same From Idrisy et al. 2015), and Tidal Deformability of 400

EOS	$M_{\max}$	$R_{1.4M_\odot}$	$\kappa_{.15C}$ (Idrisy et al. 2015)	$\kappa_{400\Lambda}$
SLY	2.05	11.77	0.573(0.587)	0.558
AP3	2.39	12.06	0.572(0.588)	0.555
AP4	2.21	11.40	0.571(0.587)	0.557
ALF2	2.09	13.18	0.571(0.588)	0.552
WFF1	2.13	10.40	0.572(0.587)	0.551
WFF2	2.20	11.14	0.571(0.587)	0.554
MPA1	2.46	12.48	0.571(0.588)	0.553
ENG	2.25	12.08	0.572(0.588)	0.546
H4	2.03	12.95	0.573(0.591)	0.552
DD2	2.42	13.04	0.572(-)	0.554
BSK22	2.26	12.73	0.571(-)	0.554
SLY9	2.16	12.20	0.574(-)	0.555
QHC19	2.18	11.35	0.574(-)	0.553
CMF5	2.07	12.87	0.573(-)	0.554
SKI4	2.17	12.10	0.574(-)	0.556

Idrisy et al. (2015), a detailed discussion on the range of possible NSs is given in Section 5. In Figure 5, we plot the r-mode frequency κ versus compactness for all 15 EOSs and see that κ does not change much as a function of compactness for different EOSs. We use a quadratic fit with the zeroth term fixed to its Newtonian value $2/3$ and get the universal relation for κ versus compactness C as

$$\kappa = 0.667 - 0.478C - 1.11C^2. \quad (39)$$

To compare the results from Gupta et al. (2022) and Ma et al. (2021), where they looked for possible resonant r-mode detection in the inspiral phase of the binary mergers using the third-generation detector Einstein telescope, in Figure 6 we plot κ as a function of $\log(\Lambda)$ for all 15 EOSs and fit it to a quadratic model without any physical restrictions on the coefficients. The corresponding universal relation is given by

$$\kappa = 0.3446 + 0.0471\log(\Lambda) - 0.002\log^2(\Lambda). \quad (40)$$

Comparing the result from Gupta et al. (2022), we get around 5%–6% difference in the r-mode frequency for a given tidal deformability. In Table 1, we also report the value of r-mode frequency κ for a compactness of 0.15 and a tidal deformability of 400 for each of the 15 EOSs.

4.2.2. Nonparametric EOS Model

Several different parameterizations of the NS EOS have been proposed to constrain the EOS from multimessenger observations of the NSs. Generic parameterizations in terms of piecewise polytropes (Read et al. 2009; Hebeler et al. 2013; Annala et al. 2018; Gamba et al. 2019), spectral decomposition (Lindblom 2018; Fasano et al. 2019), and speed of sound (Tews et al. 2018; Greif et al. 2019) have been extensively used for such studies. Here we consider the

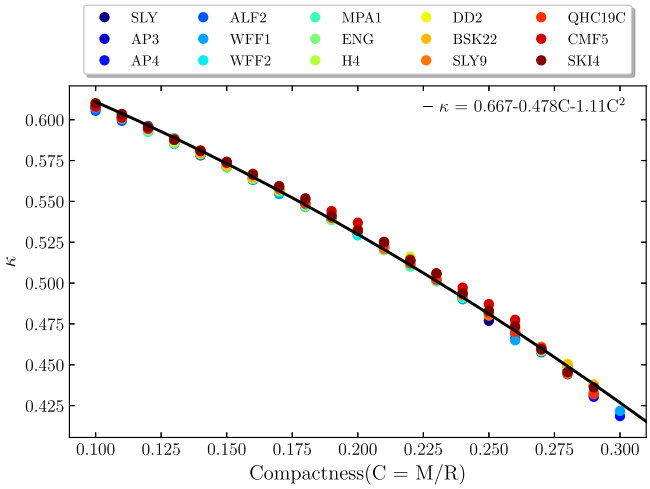

Figure 5. κ vs. compactness results for all 15 tabulated EOSs. The black line represents the best fit to our quadratic model.

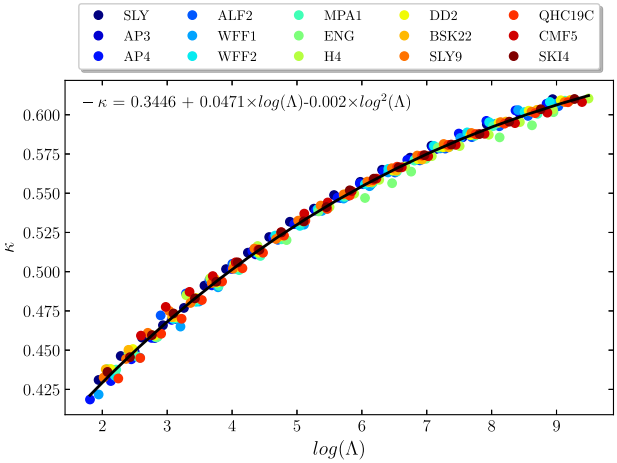

Figure 6. κ vs. $\log(\Lambda)$ results for all 15 tabulated EOSs. The black line represents the best fit to our quadratic model.

nonparametric representation constructed through the Gaussian process (Landry & Essick 2019; Essick et al. 2020) rather than a parameterization for the EOS. This EOS representation allows more model freedom and can account for different degrees of freedom. In Legred et al. (2021), using this model, they studied the implications of the following multimessenger observations for the NS EOS:

1. the radio mass measurements for J0348+0432 (Antoniadis et al. 2013) and J0740+6620 (Cromartie et al. 2019; Fonseca et al. 2021);
2. the GW mass and tidal deformability measurements from GW170817 (Abbott et al. 2017, 2018, 2019) and GW190425 (Abbott et al. 2020a); and
3. mass and radius constraints from NICER observations of J0030+0451 (Miller et al. 2019; Riley et al. 2019) and J0740+6620 (Miller et al. 2021; Riley et al. 2021).

Using these combined radio, GW, and X-ray data, they put constraints for the microscopic EOS and the macroscopic NS properties, masses, radii, and tidal deformabilities. In Figure 7, we plot the 95% confidence interval for the pressure–energy density relation using the posterior obtained by combining all the constraints (Legred et al. 2022). From this posterior set of

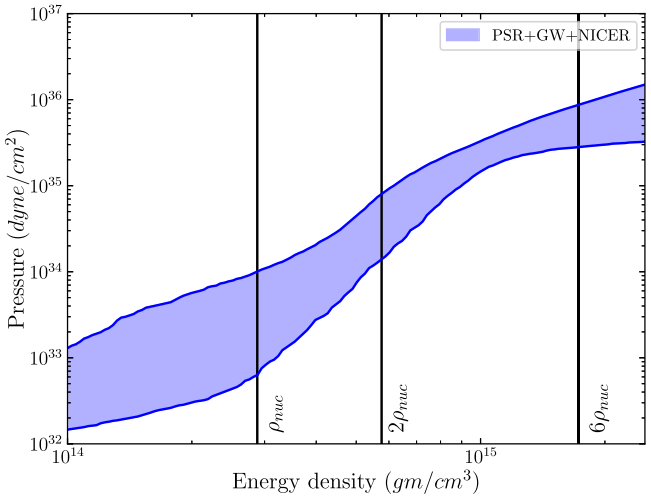

Figure 7. 95% confidence interval for pressure–density relation for nonparametric EOSs with constraints from GW, NICER, and pulsar (PSR) mass measurement.

10,000 EOSs, we choose 1000 EOSs randomly and calculate the r-mode frequency as a function of compactness and tidal deformability. In Figure 8, we plot the 95% confidence interval for the r-mode frequency κ as a function of compactness and tidal deformability. We find a substantial spread unlike Figure 5 for tabulated EOSs owing to the fact that we now have considered 1000 EOSs that span a wide region in the pressure–density relation in Figure 7.

The best fits for the r-mode frequency κ to our quadratic models are given by

$$\kappa = 0.67 - 0.593C - 0.772C^2, \tag{41}$$

$$\kappa = 0.3517 + 0.0463\,\log(\Lambda) - 0.0019\,\log^2(\Lambda). \tag{42}$$

5. Discussion and Conclusion

In this work, we solved perturbation equations for relativistic barotropic stars consistently with the boundary conditions using a spectral method and calculated the r-mode frequency as a function of compactness for various EOSs. First, we checked the convergence of our code, and then we compared our results for $n = 0$ polytropes with Figure 1 from Lockitch et al. (2003) and for $n = 1$ polytropes with Figure 2 from Idrisy et al. (2015). We see that our results match up to 0.1% for $n = 0$ polytropes from Lockitch et al. (2003). Since the precision of the converged κ value in our case is up to three decimal places, an error of the order $\leqslant$1% is expected. But we see a greater deviation $\sim$2%–3% for the results for $n = 1$ polytropes from Idrisy et al. (2015). The probable reason for this much larger deviation could be an erroneous representation of the perturbation equation, Equation (41) in Idrisy et al. (2015), where an extra r^2 term is inserted, and the boundary condition, Equation (50) in Idrisy et al. (2015), where the parity of the perturbation variables is reversed, in comparison to Equations (20) and (A4) in Lockitch et al. (2003), respectively. From Table 1 we find that, while considering the realistic EOS tables, there is also around 3% deviation in the r-mode frequency from Idrisy et al. (2015).

To get the frequency band to look for r-modes from astrophysical sources, we should consider the spread of compactness in the NS population. The compactness is estimated by the ratio of its stellar mass to the radius

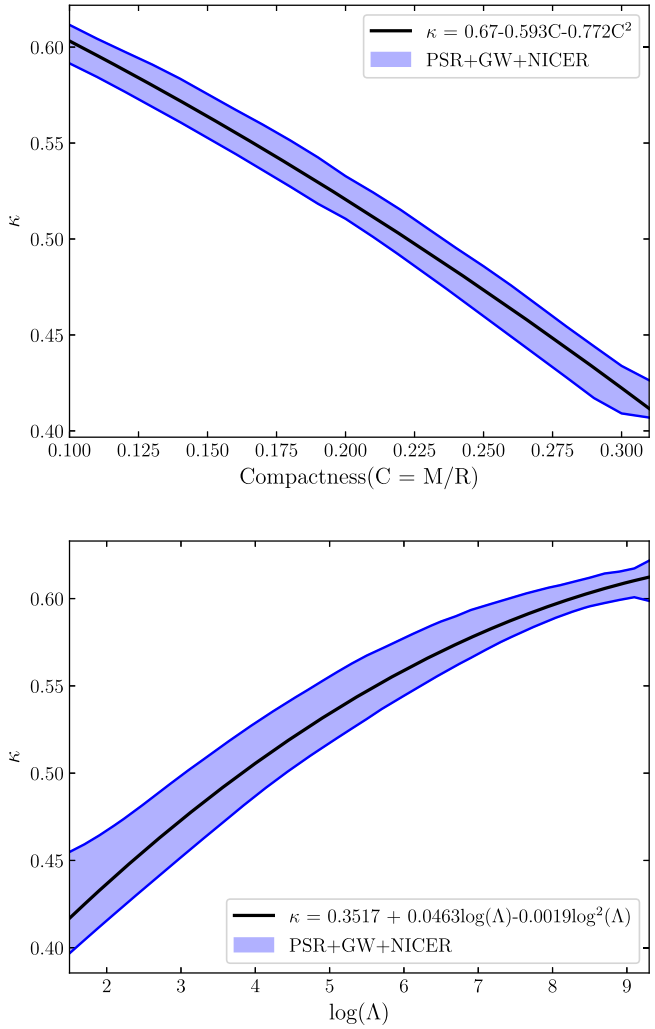

Figure 8. The top panel shows the 95% level of the r-mode frequency for a range of compactness for the nonparametric EOS models and the best quadratic model fit to the posterior. The bottom panel shows the same as the top panel, but as a function of tidal deformability.

(Idrisy et al. 2015)

$$\frac{M}{R} \approx 0.207\left(\frac{M}{1.4\,M_\odot}\right)\left(\frac{10\text{ km}}{R}\right). \tag{43}$$

The minimum value of NS mass is taken to be 1 $M_\odot$ from Figure 1 of Lattimer & Prakash (2010). The limit is conservative in a sense that stellar cores with lesser mass probably would not go through supernova explosion to produce NSs. For our set of tabulated EOSs listed in Table 1, we find the maximum radius for 1 $M_\odot$ stars to be around 14.5 km. This gives the lower limit of compactness to be $\approx$0.103. Assuming the causality of EOSs, there is an upper limit to the compactness $\frac{M}{R} \leqslant 0.35$ (Lattimer & Prakash 2007), but none of the EOSs from Table 1 reach this high value for any stable configuration. Idrisy et al. (2015) use the compactness range 0.11–0.31, but we give our limits of the r-mode frequency for both compactness ranges in Table 2.

Now, to calculate the narrow frequency band to search over in LIGO data, the r-mode frequency (f) is given in terms of the rotational frequency (ν) (Caride et al. 2019;

Table 2
Proposed Ranges of κ and A (Caride et al. 2019) for Ranges of Compactness Comparing Universal Relations from Idrisy et al. (2015) with Our Results for Both Tabulated EOSs and Nonparametric EOSs

Universal Relation (Compactness Range)	κ	A
(Idrisy et al. 2015) (0.11–0.31)	0.614–0.433	1.39–1.57
Tabulated EOS (39) (0.11–0.31)	0.601–0.412	1.40–1.59
Tabulated EOS (39) (0.10–0.35)	0.608–0.364	1.39–1.64
Nonparametric EOS (41) (0.11–0.31)	0.596–0.415	1.39–1.59
Nonparametric EOS (41) (0.10–0.35)	0.604–0.371	1.40–1.63

Abbott et al. 2021) as

$$\frac{f}{\nu} = A - B\left(\frac{\nu}{\nu_{\rm K}}\right)^2, \tag{44}$$

where $\nu_{\rm K}$ is the Keplerian frequency $= 506$ Hz considered in Abbott et al. (2021). The uncertainties in the range of A and B give the parameter space for the GW signal model (Caride et al. 2019; Abbott et al. 2021). General relativistic corrections for slowly rotating stars give the range of A (Idrisy et al. 2015), and rapid rotation correction gives the range of B (Yoshida et al. 2005). The ranges are given by (Caride et al. 2019)

$$\begin{aligned} 1.39 \leqslant A \leqslant 1.57, \\ 0 \leqslant B \leqslant 0.195. \end{aligned} \tag{45}$$

Since the r-mode frequency in the inertial frame is given by $f = |(\kappa - m)\Omega|$, we can use the limits on κ to update the limits on A value, which is also listed in Table 2. Considering all these multimessenger constraints and a conservative limit on the possible ranges of compactness, we put a limit on the value of A of $1.39 \leqslant A \leqslant 1.64$, which should be used for narrowband GW searches for known pulsars.

Although we use very different fitting formulae for κ from Idrisy et al. (2015) as described in Section 1, we end up with similar ranges for the parameter A. In particular, Idrisy et al. (2015) had a positive value for the linear in M/R term in Equation (2), while we had a negative one, and the zeroth-order term we fixed to the Newtonian value, which is slightly higher than the same used by Idrisy et al. (2015). These two changes actually counter each other, and the net effect is to give results for κ that are not significantly different over the relevant range in compactness ($\sim$0.1–0.35).

PSR J0537–6910 is particularly interesting for r-mode searches because it is the fastest-spinning known young pulsar with rotation frequency $\nu = 62$ Hz, which places GW frequency in the LIGO sensitivity band, and its interglitch braking index $n \approx 7$, which is expected for GW emission via r-mode (Andersson et al. 2018). In the latest LIGO r-mode search from PSR J0537, values of A and B in Equation (45) give the r-mode frequency band 86–98 Hz. If we use our universal relation (39) for a compactness range of 0.11–0.31 (same as in Idrisy et al. 2015), we get the frequency band 87–99 Hz, which is 1 Hz higher in both lower and upper bounds. Although the bandwidth remains the same, this new universal relation introduces a 1% change in the mean frequency of the band. For a compactness range of 0.10–0.35, this range becomes 86–101 Hz, which is 25% higher compared to the previous search bandwidths.

We also provided universal relations for the r-mode frequency κ and the dimensionless tidal deformability (Λ) in Equations (40) and (42). Recent work by Gupta et al. (2022) used such a relation to reconstruct the EOS with observations of the inspiral signal by the Einstein telescope with or without r-modes. They used the universal relation for κ versus compactness from Idrisy et al. (2015) to derive the r-mode frequency as a function of $\log(\Lambda)$. If we compare Equation (7) from Gupta et al. (2022) against our universal relation, we observe a 5%–6% difference in the r-mode frequency, which can be significant while constraining the nuclear EOS from inspiral signal with r-modes.

To conclude, we have derived the r-mode frequency as a function of compactness for NSs and showed that one can obtain a universal relation between r-mode frequency and the compactness that is independent of the EOSs. With a physically motivated range of compactness, we derived the frequency band to search for r-modes in the LIGO data. For the particularly interesting candidate PSR J0537–6910, we showed that our narrowband frequency range can vary from the previous searches by up to 25% depending on the compactness range chosen. If a continuous wave from r-mode is detected, these universal relations can also be used to constrain the nuclear EOS, but distinguishing between different EOSs will be difficult, as the deviation in r-mode frequency is $<1\%$ for different EOSs. Using the Einstein telescope, if r-mode excitation is observed in the inspiral signal, we also can constrain the tidal deformability and the EOS using our universal relations. Although in this study we ignored rapid rotation and other physical mechanisms inside the NS that can affect the r-mode frequency, they might be important for some particular NSs, and in the future we would like to explore how these mechanisms affect r-mode frequency for different EOSs.

The authors would like to thank David Ian Jones for his useful comments and suggestions on the material of this paper. S.G. would like to thank Bikram Keshari Pradhan for useful discussions during this work. The authors acknowledge usage of the IUCAA HPC computing facility for the numerical calculations.

ORCID iDs

Suprovo Ghosh https://orcid.org/0000-0002-1656-9870
Dhruv Pathak https://orcid.org/0000-0001-8129-0473
Debarati Chatterjee https://orcid.org/0000-0002-0995-2329

References

Aasi, J., Abbott, B. P., Abbott, R., et al. 2015, CQGra, 32, 074001
Abbott, B., Abbott, R., Abbott, T., et al. 2017, PhRvL, 119, 161101
Abbott, B., Abbott, R., Abbott, T., et al. 2018, PhRvL, 121, 161101
Abbott, B., Abbott, R., Abbott, T., et al. 2019, PhRvX, 9, 011001
Abbott, B., Abbott, R., Abbott, T., et al. 2020a, ApJL, 892, L3
Abbott, B., Abbott, R., Abbott, T., et al. 2020b, CQGra, 37, 045006
Abbott, B., Abbott, R., Abbott, T., et al. 2022, PhRvD, 105, 022002
Abbott, B. P., Abbott, R., Abbott, T. D., et al. 2016, PhRvL, 116, 131103
Abbott, R., Abbott, T. D., Abraham, S., et al. 2021, ApJ, 922, 71
Acernese, F., Agathos, M., Agatsuma, K., et al. 2014, CQGra, 32, 024001
Akutsu, T., Ando, M., Arai, K., et al. 2021, PTEP, 2021, 05A101
Alford, M. G., & Schwenzer, K. 2014, ApJ, 781, 26
Andersson, N. 1998, ApJ, 502, 708
Andersson, N. 2003, CQGra, 20, R105

Andersson, N., Antonopoulou, D., Espinoza, C. M., Haskell, B., & Ho, W. C. G. 2018, ApJ, 864, 137
Andersson, N., & Comer, G. 2001, MNRAS, 328, 1129
Andersson, N., Kokkotas, K., & Schutz, B. F. 1999, ApJ, 510, 846
Annala, E., Gorda, T., Kurkela, A., & Vuorinen, A. 2018, PhRvL, 120 172703
Antoniadis, J., Freire, P. C. C., Wex, N., et al. 2013, Sci, 340, 1233232
Baym, G., Furusawa, S., Hatsuda, T., Kojo, T., & Togashi, H. 2019, ApJ, 885, 42
Biswas, B. 2022, ApJ, 926, 75
Biswas, B., Char, P., Nandi, R., & Bose, S. 2021, PhRvD, 103, 103015
Caride, S., Inta, R., Owen, B. J., & Rajbhandari, B. 2019, PhRvD, 100, 064013
Chandrasekhar, S. 1970, PhRvL, 24, 611
Chatterjee, D., & Bandyopadhyay, D. 2006, PhRvD, 74, 023003
Chatterjee, D., & Bandyopadhyay, D. 2007, PhRvD, 75, 123006
Cromartie, H. T., Fonseca, E., Ransom, S. M., et al. 2019, NatAs, 4, 72
Dexheimer, V., & Schramm, S. 2008, ApJ, 683, 943
Dietrich, T., Coughlin, M. W., Pang, P. T. H., et al. 2020, Sci, 370, 1450
Essick, R., Landry, P., & Holz, D. E. 2020, PhRvD, 101, 063007
Fasano, M., Abdelsalhin, T., Maselli, A., & Ferrari, V. 2019, PhRvL, 123, 141101
Fesik, L., & Papa, M. A. 2020a, ApJ, 895, 11
Fesik, L., & Papa, M. A. 2020b, ApJ, 897, 185
Flanagan, E. E., & Hinderer, T. 2008, PhRvD, 77, 021502
Fonseca, E., et al. 2021, ApJL, 915, L12
Friedman, J. L., & Schutz, B. F. 1978, ApJ, 222, 281
Gamba, R., Read, J. S., & Wade, L. E. 2019, CQGra, 37, 025008
Ghosh, S., Chatterjee, D., & Schaffner-Bielich, J. 2022, EPJA, 58, 37
Glendenning, N. 2012, Compact Stars: Nuclear Physics, Particle Physics and General Relativity (New York: Springer)
Greif, S. K., Raaijmakers, G., Hebeler, K., Schwenk, A., & Watts, A. L. 2019, MNRAS, 485, 5363
Gupta, P. K., Puecher, A., Pang, P. T. H., et al. 2022, arXiv:2205.01182
Hartle, J. B. 1967, ApJ, 150, 1005
Hebeler, K., Lattimer, J. M., Pethick, C. J., & Schwenk, A. 2013, ApJ, 773, 11
Hild, S., Abernathy, M., Acernese, F., et al. 2011, CQGra, 28, 094013
Hinderer, T. 2008, ApJ, 677, 1216
Ho, W. C. G., Andersson, N., & Haskell, B. 2011, PhRvL, 107, 101101
Ho, W. C. G., & Lai, D. 2000, ApJ, 543, 386
Idrisy, A., Owen, B. J., & Jones, D. I. 2015, PhRvD, 91, 024001
Landry, P., & Essick, R. 2019, PhRvD, 99, 084049
Lattimer, J. M., & Prakash, M. 2007, PhR, 442, 109
Lattimer, J. M., & Prakash, M. 2010, What a Two Solar Mass Neutron Star Really Means (Singapore: World Scientific)
Legred, I., Chatziioannou, K., Essick, R., Han, S., & Landry, P. 2021, PhRvD, 104, 063003
Legred, I., Chatziioannou, K., Essick, R., Han, S., & Landry, P. 2022, Impact of the PSR J0740+6620 Radius Constraint on the Properties of High-density Matter: Neutron Star Equation of State Posterior Samples, Zenodo doi:10.5281/zenodo.6502467
Levin, Y., & Ushomirsky, G. 2001, MNRAS, 324, 917
2018, LIGO Scientific Collaboration, LIGO Algorithm Library—LALSuite, Free Software (GPL), 10.7935/GT1W-FZ16
Lindblom, L. 2018, PhRvD, 97, 123019
Lindblom, L., & Mendell, G. 2000, PhRvD, 61, 104003
Lindblom, L., Mendell, G., & Owen, B. J. 1999, PhRvD, 60, 064006
Lindblom, L., & Owen, B. J. 2002, PhRvD, 65, 063006
Lindblom, L., Owen, B. J., & Morsink, S. M. 1998, PhRvL, 80, 4843
Lockitch, K. H., Andersson, N., & Friedman, J. L. 2000, PhRvD, 63, 024019
Lockitch, K. H., Friedman, J. L., & Andersson, N. 2003, PhRvD, 68, 124010
Ma, S., Yu, H., & Chen, Y. 2021, PhRvD, 103, 063020
Miller, M. C., Lamb, F. K., Dittmann, A. J., et al. 2019, ApJL, 887, L24
Miller, M. C., Lamb, F. K., Dittmann, A. J., et al. 2021, ApJL, 918, L28
Morsink, S. M., & Rezania, V. 2002, ApJ, 574, 908
Oertel, M., Hempel, M., Klaehn, T., & Typel, S. 2017a, CompOSE, https://compose.obspm.fr/
Oertel, M., Hempel, M., Klaehn, T., & Typel, S. 2017b, RvMP, 89, 015007
Özel, F., & Freire, P. 2016, ARA&A, 54, 401
Pang, P. T. H., Tews, I., Coughlin, M. W., et al. 2021, ApJ, 922, 14
Papaloizou, J., & Pringle, J. E. 1978, MNRAS, 182, 423
Passamonti, A., Haskell, B., Andersson, N., Jones, D. I., & Hawke, I. 2009, MNRAS, 394, 730
Provost, J., Berthomieu, G., & Rocca, A. 1981, A&A, 94, 126
Punturo, M., Abernathy, M., Acernese, F., et al. 2010, CQGra, 27, 084007
Rajbhandari, B., Owen, B. J., Caride, S., & Inta, R. 2021, PhRvD, 104, 122008
Read, J. S., Lackey, B. D., Owen, B. J., & Friedman, J. L. 2009, PhRvD, 79, 124032
Rezzolla, L., Lamb, F. K., Marković, D., & Shapiro, S. L. 2001a, PhRvD, 64, 104013
Rezzolla, L., Lamb, F. K., Marković, D., & Shapiro, S. L. 2001b, PhRvD, 64, 104014
Rezzolla, L., Lamb, F. K., & Shapiro, S. L. 2000, ApJL, 531, L139
Riley, T. E., Watts, A. L., Bogdanov, S., et al. 2019, ApJL, 887, L21
Riley, T. E., Watts, A. L., Ray, P. S., et al. 2021, ApJL, 918, L27
Tews, I., Margueron, J., & Reddy, S. 2018, PhRvC, 98, 045804
Tong, H., Zhao, P., & Meng, J. 2020, PhRvC, 101, 035802
Traversi, S., Char, P., & Pagliara, G. 2020, ApJ, 897, 165
Yoshida, S., & Lee, U. 2000, ApJS, 129, 353
Yoshida, S., Yoshida, S., & Eriguchi, Y. 2005, MNRAS, 356, 217